

Article

Study of Air Pressure and Velocity for Solution Blow Spinning of Polyvinylidene Fluoride Nanofibres

Rasheed Atif ¹, Madeleine Combrinck ², Jibran Khaliq ², James Martin ², Ahmed H. Hassanin ^{3,4,5}, Nader Shehata ^{3,6,7,8}, Eman Elnabawy ³ and Islam Shyha ^{1,*}

- ¹ Mechanical Engineering and Design, School of Engineering and the Built Environment, Merchiston Campus, Edinburgh Napier University, Edinburgh EH10 5DT, UK; A.Rasheed@napier.ac.uk
- ² Department of Mechanical and Construction Engineering, Faculty of Engineering and Environment, Northumbria University, Newcastle upon Tyne NE1 8ST, UK; madeleine.combrinck@northumbria.ac.uk (M.C.); jibran.khaliq@northumbria.ac.uk (J.K.); james.e.martin@northumbria.ac.uk (J.M.)
- ³ Centre of Smart Nanotechnology and Photonics (CSNP), SmartCI Research Centre, Alexandria University, Alexandria 21544, Egypt; ahmed.hassanin@ejust.edu.eg (A.H.H.); nader83@vt.edu (N.S.); eman.elnabawy@smartci.alexu.edu.eg (E.E.)
- ⁴ Department of Textile Engineering, Faculty of Engineering, Alexandria University, Alexandria 21544, Egypt
- ⁵ Materials Science & Engineering Department, School of Innovative Design Engineering, Egypt-Japan University of Science and Technology (E-JUST), 179 New Borg El-Arab City, Alexandria 21934, Egypt
- ⁶ Department of Engineering Mathematics and Physics, Faculty of Engineering, Alexandria University, Alexandria 21544, Egypt
- ⁷ USTAR Bioinnovations Centre, Faculty of Science, Utah State University, Logan, UT 84341, USA
- ⁸ Kuwait College of Science and Technology (KCST), Doha District 13133, Kuwait
- * Correspondence: I.Shyha@napier.ac.uk; Tel.: +44-(0)1-314-552-624

Citation: Atif, R.; Combrinck, M.; Khaliq, J.; Martin, J.; Hassanin, A.H.; Shehata, N.; Elnabawy, E.; Shyha, I. Study of Air Pressure and Velocity for Solution Blow Spinning of Polyvinylidene Fluoride Nanofibres. *Processes* **2021**, *9*, 1014. <https://doi.org/10.3390/pr9061014>

Academic Editor: Alfredo Iranzo

Received: 30 April 2021

Accepted: 2 June 2021

Published: 8 June 2021

Publisher's Note: MDPI stays neutral with regard to jurisdictional claims in published maps and institutional affiliations.



Copyright: © 2021 by the authors. Licensee MDPI, Basel, Switzerland. This article is an open access article distributed under the terms and conditions of the Creative Commons Attribution (CC BY) license (<http://creativecommons.org/licenses/by/4.0/>).

Abstract: Solution blow spinning (SBS) is gaining popularity for producing fibres for smart textiles and energy harvesting due to its operational simplicity and high throughput. The whole SBS process is significantly dependent on the characteristics of the attenuation force, i.e., compressed air. Although variation in the fibre morphology with varying air input pressure has been widely investigated, there is no available literature on the experimentally determined flow characteristics. Here, we have experimentally measured and calculated airflow parameters, namely, output air pressure and velocity in the nozzle wake at 12 different pressure values between 1 and 6 bar and 11 different positions (retracted 5 mm to 30 mm) along the centreline. The results obtained in this work will answer many critical questions about optimum protrusion length for the polymer solution syringe and approximate mean fibre diameter for polyvinylidene fluoride (PVDF) at given output air pressure and velocity. The highest output air pressure and velocity were achieved at a distance of 3–5 mm away from the nozzle wake and should be an ideal location for the apex of the polymer solution syringe. We achieved 250 nm PVDF fibres when output air pressure and velocity were 123 kPa and 387 m/s, respectively.

Keywords: solution blow spinning (SBS); air pressure and velocity; computational fluid dynamics (CFD); polyvinylidene fluoride (PVDF); energy harvesting

1. Introduction

The solution blow spinning (SBS) technique has two main advantages over its competitor electrospinning: Firstly, it does not require an electric field, and secondly, its throughput can be two orders of magnitude higher than that of electrospinning [1–5]. SBS process is also very simple since it mainly contains compressed air that passes through a nozzle and attenuates polymer solution droplet converting it into a fibre. The fluid flow characteristics are significantly dependent on the nozzle design. Park and Reitz [6]

employed a jet superposition modelling approach using an equation they derived based on the law of conservation of momentum and then used that equation as a sub-grid-scale sub-model in a Lagrangian Drop–Eulerian Gas CFD model. They reported that when the angle of convergence increases, spray cross section becomes ellipsoidal, and the air entrainment becomes more conspicuous. The air entrainment can affect the droplets' size range since it can favour collision, resulting in either division or coalescence. The droplet size is an essential parameter in fibre spinning because it dictates the diameter of the produced fibre.

Similarly, nozzle diameter also influences the fibre spinning process. Morrall et al. carried out Reynolds-averaged Navier–Stokes (RANS) simulations based on k – ω shear stress transport and the Reynolds stress models [7]. They reported that nozzle diameter significantly influences the flow swirl and head losses in the nozzle. A stronger flow swirl retains jet energy for a longer duration that helps in the thorough mixing of the fluids coming out of the nozzle. The prolonged interaction time can aid in more extensive stretching in the fibre resulting in thinner fibres and can help in rapid evaporation of the solvent in the polymer solution, resulting in comparatively dry fibres. They further reported that although both tested models predict flow characteristics that are in good agreement with the experimental results; however, at higher flow swirls, the Reynolds stress model appears to be more accurate.

Although the SBS process has been mainly carried out at room temperature, the inflow temperature can be an interesting parameter to investigate. Xue et al. carried out CFD simulations of spray nozzles using mixture models and reported that the discharge coefficient is dependent on the inflow temperature, and as the inflow temperature increases, the discharge coefficient decreases [8]. They further observed that higher inflow temperatures lead to higher cavitation intensity, higher saturation pressure, and an increased vapour phase concentration at the nozzle's exit point. Such factors can significantly reduce the mass flow rate. The heating of the compressed gas interacting with the polymer solution can cause it to dry quickly. In the case of polyvinylidene fluoride (PVDF), the polymer solution is generally comprised of 10–20 wt/vol%, which means that there is 80–90% of organic solvent that needs to be removed entirely from the spun fibres since any retained solvent or volatiles can degrade both mechanical and piezoelectric properties [9]. Hot compressed air can aid in obtaining solvent-free dry fibres.

Since air is the only attenuation force, the fibre morphology is significantly dependent on the airflow characteristics. If air does not have significant pressure and velocity to overcome surface tension, the polymer droplet will not elongate but rather solidify as a spherical particle [10–13]. Therefore, the input air pressure and related velocity should be above a specific threshold value depending on the polymer type, viscosity of the polymer solution, and diameter of the droplet. The mean fibre diameter should then intuitively decrease with increasing input air pressure and related velocity. However, the more the input air pressure and corresponding velocity are, the more turbulent the flow will be. This turbulence might cause random and localised variations in the fibre diameter or even break the fibres [14]. Therefore, it is important to determine an optimum input air pressure and related velocity under a given set of conditions. This makes the investigation of the airflow fields important.

In this work, we have investigated the airflow field using a pitot tube and a manometer and compared the results with computational fluid dynamics (CFD) results based on the k – ϵ turbulence model. We have then approximated the flow characteristics with the mean fibre diameter based on experimentally produced PVDF nanofibres.

2. Materials and Methods

A schematic diagram showing the procedure to measure dynamic pressure and data logging is presented in Figure 1, and the experimental setup is shown in Figure 2. Two different datasets were acquired with the central nozzle hole, as shown in Figure 2 (inset)

where polymer solution syringe was stationed, completely blocked for the first dataset, and fully opened for the other dataset. A Bambi air compressor (VTS 150D, Bambi, Newcastle upon Tyne, UK) was used to provide oil-free dry air. An SBS nozzle was clamped on a stand and air was supplied through a 6 mm internal diameter hose. To measure the centreline dynamic air pressure coming out of the nozzle, a pitot tube with an inner diameter of 0.4 mm and an external diameter of 0.7 mm was positioned right in front of the nozzle end. The distance between the tip of the pitot tube and the nozzle was varied and pressure was measured at 11 different locations, as shown in Figure 3. Due to its small size, the pitot tube could be inserted into the nozzle (Figure 3a). It was positioned 5 mm inside the nozzle and called -5 mm, where the minus sign indicates retraction. The second measurement was made right at the tip of the nozzle end with a distance of 0 mm. The following nine readings were made at distances of 1, 2, 3, 5, 7, 10, 15, 20, and 30 mm. The pitot tube was connected to the positive terminal of the manometer (TPI 665), while the negative terminal was exposed to the atmosphere and hence dynamic pressure was recorded. To achieve continuous digital values, a manometer was connected to a laptop, and the frequency of data logging was 1 Hz. From the dynamic pressure, air velocity was calculated using Equation (1).

$$\frac{1}{2} \rho v^2 = \frac{\gamma}{\gamma - 1} p \left[\left(\frac{p_0}{p} \right)^{(\gamma-1)/\gamma} - 1 \right] \quad (1)$$

where ρ is air density (1.225 kg/m³), v is the air velocity, γ is the ratio of specific heats (1.4 for air), p is the dynamic pressure, and p_0 is the total pressure. The values obtained were compared with the $k-\epsilon$ turbulence model based on CFD results and the mean fibre diameter of PVDF. A detailed description of the CFD method and production of PVDF nanofibres is provided elsewhere [15] and will not be repeated here for the sake of brevity.

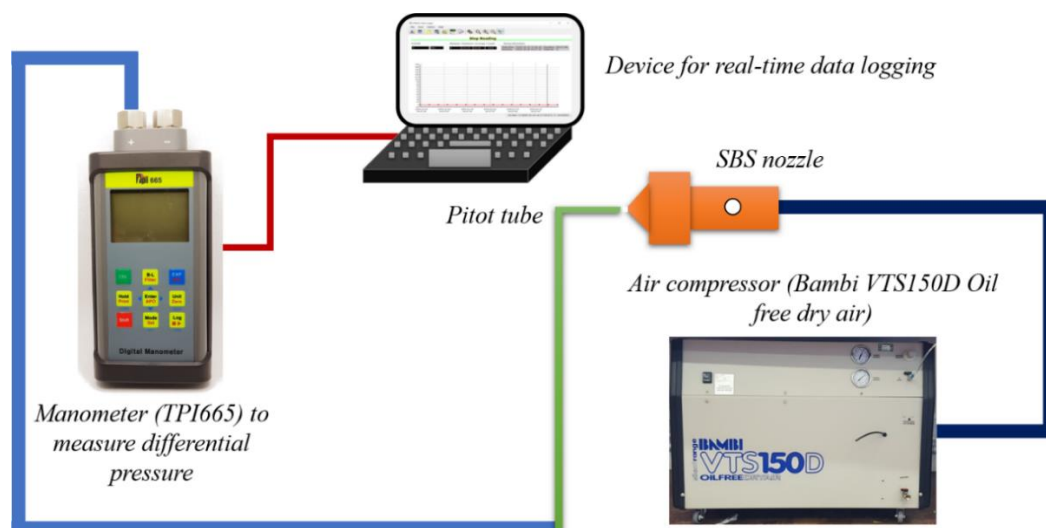


Figure 1. A schematic diagram showing the setup to measure the airflow field as it exists the SBS nozzle.



Figure 2. The experimental setup consisting of the pitot tube, SBS nozzle, manometer, and laptop for data logging. Inset shows the central nozzle hole and four side holes for air.

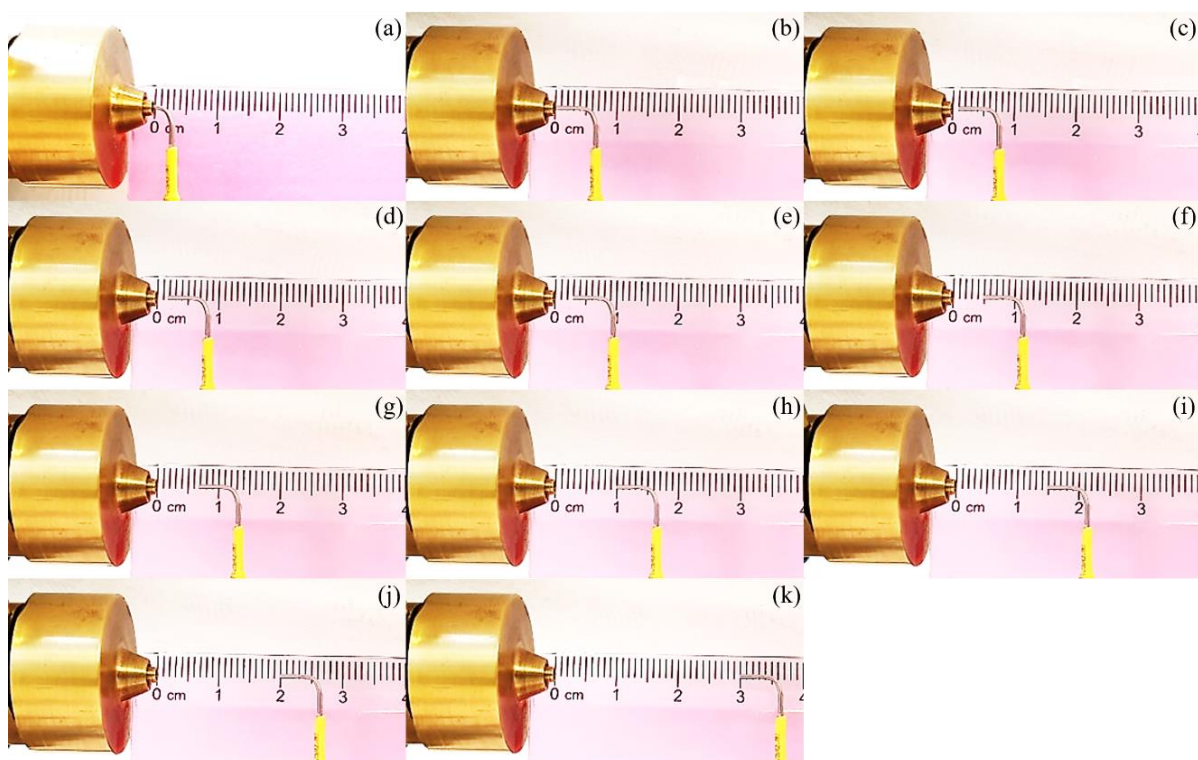


Figure 3. Varying distance between pitot tube and the nozzle outlet: (a) -5 mm (negative sign shows that the pitot tube is inside the nozzle), (b) 0 mm, (c) 1 mm, (d) 2 mm, (e) 3 mm, (f) 5 mm, (g) 7 mm, (h) 10 mm, (i) 15 mm, (j) 20 mm, and (k) 30 mm.

3. Results and Discussion

When the pitot tube was inside the nozzle, only negative pressure values were recorded, confirming that no air passed through the central hole. The air coming out through the annulus around the central hole caused a negative air pressure, and CFD demonstrated this phenomenon as reverse flow [15]. The variation in output air pressure along the centreline at different input air pressure values with the central hole completely blocked is shown in Figure 4. The central nozzle hole was blocked in the experimental work and simulations; therefore, the comparison charts presented are under the same

conditions. At 1 bar input air pressure, CFD predicted that output air pressure would fluctuate between 0 and 5 kPa as we move away from the nozzle end to a distance of 5 mm. The first four readings (i.e., up to 3 mm distance away from the nozzle end) of the experimentally measured output air pressure were relatively closer to CFD values. However, the experimental value at a distance of 5 mm showed a considerable jump and recorded a value of ~80 kPa, nearly equal to 0.8 bar. This value suggested that about 80% of the input air pressure was transmitted through the nozzle. A decrease of 20% can be attributed to pressure losses at the junctions, reverse flow, and turbulence.

Although achieving 80% of the input as output seemed reasonable, CFD prediction of ~0 kPa seemed highly unlikely. However, such a difference can be easily explained based on reverse flow and the limitation of the pitot tube diameter.

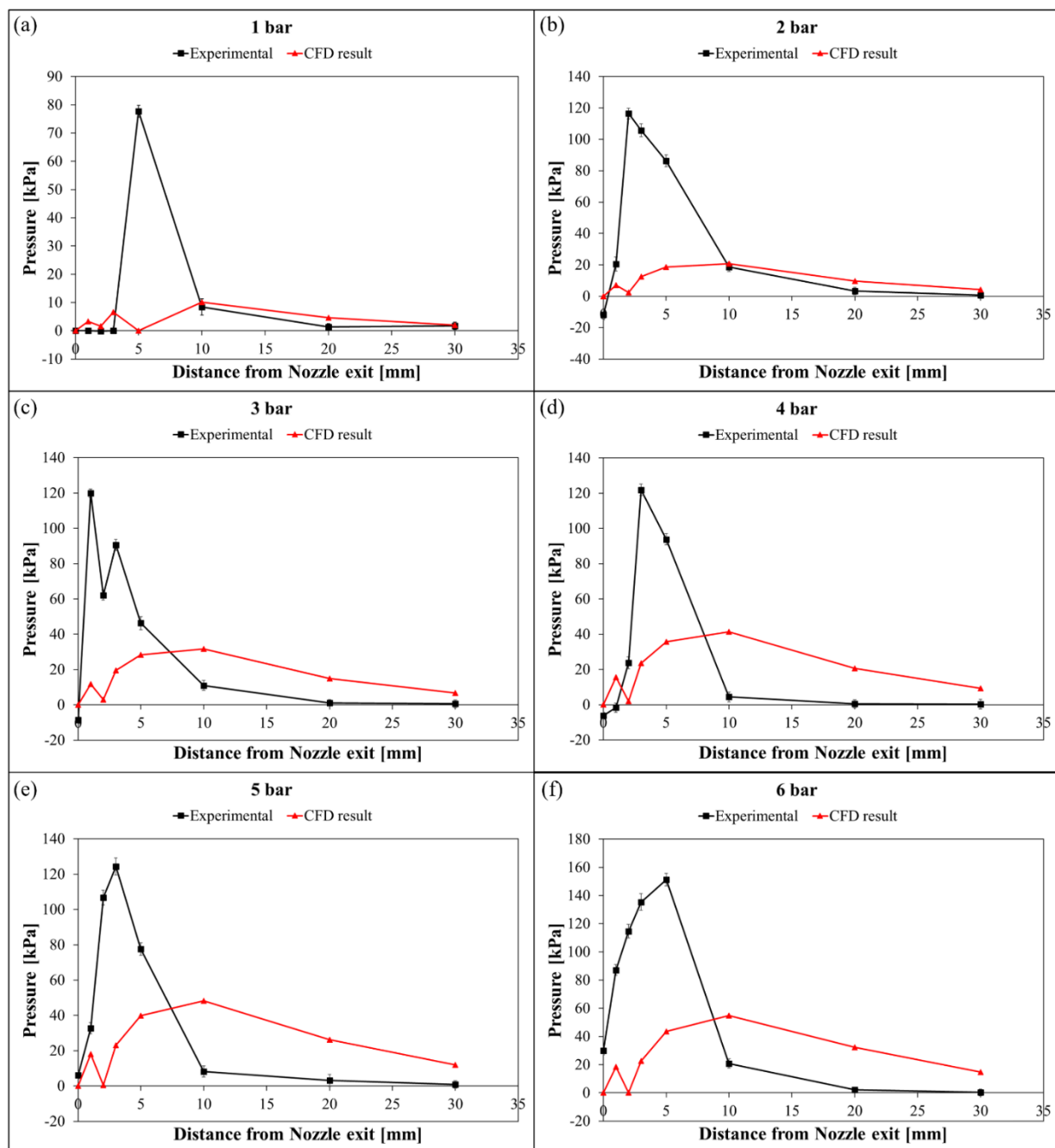


Figure 4. Comparison between CFD and experimental results for output air pressure at different input pressure values: (a) 1 bar, (b) 2 bar, (c) 3 bar, (d) 4 bar, (e) 5 bar, and (f) 6 bar.

When a fluid exited through a convergent nozzle, a reverse flow developed in the proximity of the exit point. If we were to place a pitot tube in that region, the pressure recorded could either be negative or close to zero. However, if some part of the opening of the pitot tube was outside of the reverse flow region, a positive value of pressure would be recorded. Since we observed a negative value of output air pressure (at 2, 3, and 4 bar input air pressure), it suggested that the diameter of the pitot tube was smaller than the reverse flow region. This left us assuming that the reverse flow region did not extend to 5 mm away from the nozzle end. At a distance of 10 mm away from the nozzle end, the output air pressure values plummeted to ~10 kPa. Both CFD and experimental values showed a remarkable match.

At 2 bar input air pressure, CFD predicted output air pressure value close to zero. However, the experimental value was ~-12 kPa, indicating the pitot tube was inside the reverse flow region. At a distance of 2 mm, CFD predicted a value of ~1 kPa. On the contrary, the pitot tube recorded a value of ~117 kPa, which is the highest value recorded at 2 bar. At 3 mm and 5 mm, the recorded values decreased to ~105 kPa and ~84 kPa, respectively. The CFD and experimental values remained in agreement at a distance of ≥ 10 mm. The comparative trends remained similar at higher pressures, except that CFD overestimated output air pressure values at a distance of ≥ 10 mm. This indicated that pressure decayed more rapidly in reality than that predicted by CFD. Although the $k-\epsilon$ turbulence model predicted a slow decay in the air velocity, some other theoretical studies suggest a rapid decay. Zhang et al. [16] carried out CFD of a sharp-edged nozzle using the OpenFOAM source code and reported that the axial velocity showed a rapid decay at the jet centre (within the axial distance).

The trends suggested that CFD underestimated the values of air pressure and velocity. The discrepancy resulted from the underestimation of the turbulence intensity of the nozzle in CFD simulations. Turbulence intensity represents the intensity of velocity fluctuation of a fluid. It is defined as the ratio of the standard deviation of fluctuating fluid velocity to the mean fluid speed. Some work has been recently carried out to optimise the role of turbulence intensity to better predict the overall flow characteristics [17]. The exploration into the modification of the influential parameters has led to the development of various turbulence models that can be traversed for a more accurate prediction of the flow characteristics [18,19].

The highest output pressure values were recorded outside the nozzle at around 5 mm away from the nozzle end. This is an important result since the protrusion length of the polymer solution syringe is critical in achieving a smooth and continuous process as flow is hindered in the retracted syringes and causes disruption in the process. Lou et al. [20] showed that a protrusion length of 4 mm is optimum, and our results were in close agreement.

The variation in output air velocity with input air pressure is shown in Figure 5. The air velocity could reach as high as 600 m/s. Compared to firearm muzzle velocities that range from ~100 m/s to 350 m/s, a velocity of 600 m/s can be lethal. This much high velocity can rupture the eardrum and knock the eye out of its socket. Therefore, care had to be exercised while the SBS nozzle was in operation.

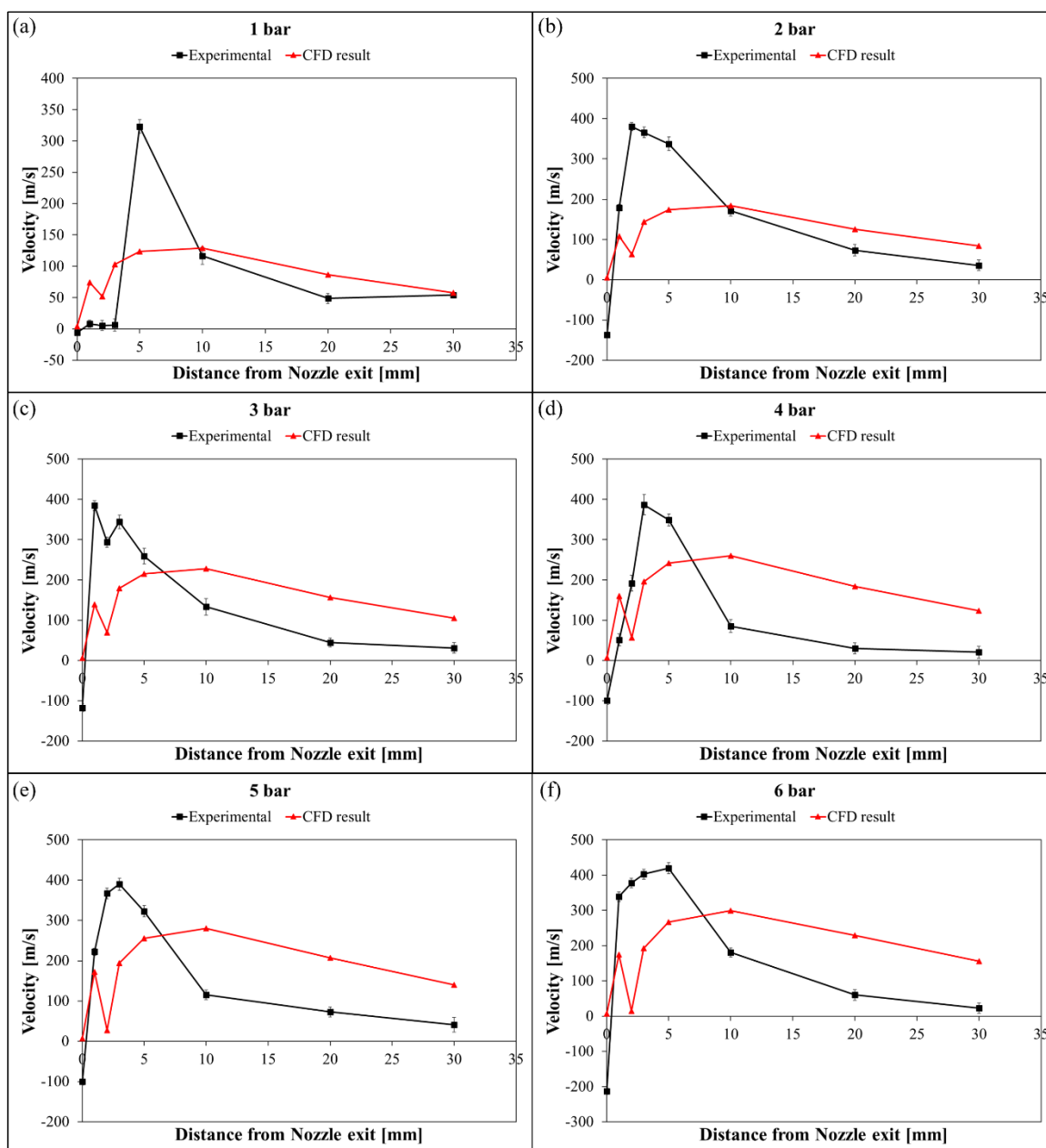


Figure 5. Comparison between CFD and experimental results for output air velocity at different input pressure values: (a) 1 bar, (b) 2 bar, (c) 3 bar, (d) 4 bar, (e) 5 bar, and (f) 6 bar.

The mean fibre diameters achieved experimentally at 2, 3, and 4 bar input air pressure were 530, 420, and 250 nm, respectively. The achieved air pressure and velocity can be correlated with the mean fibre diameter as listed in Table 1. When the air output pressure was around 117 kPa, the mean fibre diameter (15 wt % PVDF in DMF at a feed rate of 10 mL/h) was around 530 nm. Similarly, if the output air velocity was around 380 m/s, the mean fibre diameter was around 530 nm. A similar discussion extends to other pressure and velocity values, as presented in Table 1.

Table 1. Various airflow parameters and resultant mean fibre diameter.

Sr.	Input Air Pressure (bar)	Output Air Pressure (kPa)	Output Air Velocity (m/s)	Mean Fibre Diameter (nm)
1	2	117	379.9	530
2	3	121	384.4	420
3	4	123	386.9	250

At input air pressure values of ≥ 5 bar, we observed intertwined fibres rather than individual fibres separated from each other. Such variation in fibre morphology could be explained based on turbulence. When the flow rate exceeded a certain limit, it behaved more turbulent than laminar. The variation in output pressure and velocity became prominent at elevated flow rates, and input pressure ≥ 5 bar provided such conditions. This suggested that any nozzle design would limit the maximum allowable input pressure since fibre morphology depended on the air pressure or velocity as well as on the turbulence. Therefore, a trade-off was essential between pressure and turbulence to achieve fibres with suitable morphology.

The pressure values were also measured by removing the blockage from the central hole, and the manometer readings for all locations have been shown in the Supplementary Materials (Figures S1–S9). In general, the pressure values recorded were higher than those achieved with a blocked central hole. For example, at 5 bar input air pressure, the output air pressure was 124 kPa (with blocked central hole), increasing to 157 kPa after opening the central hole. Although this could be easily explained on the basis of increased mass flow rate, it suggested that the clearance between nozzle and polymer solution syringe could be an important influential factor in defining the fibre morphology. This factor has been ignored in the reviewed literature.

4. Conclusions

In this work, we built a setup to determine air pressure and velocity as the air comes out of a solution blow spinning (SBS) nozzle. The setup comprised an air compressor, SBS nozzle, pitot tube, manometer, and a laptop for real-time data logging with a frequency of 1 Hz. We determined output air pressure and calculated air velocity and compared them with computational fluid dynamics (CFD) results based on the $k-\epsilon$ turbulence model. We investigated two variables: input pressure up to 6 bar with increments of 0.5 bar and distance from the nozzle end and the selected range was -5 mm to 30 mm (minus sign shows retraction). We investigated pressure and velocity with the central hole either completely blocked or fully opened for the polymer solution syringe. When the central hole block was blocked, the maximum output air pressure was recorded at a 3–5 mm distance. On the other hand, in the case of the central hole fully opened, the maximum output air pressure mainly was recorded at a -5 mm distance. This difference in the location of maximum pressure suggested that the clearance between the nozzle and polymer solution syringe is an important influential factor. We observed that when output air pressure (velocity) values were 117 kPa (380 m/s), 121 kPa (384 m/s), and 123 kPa (387 m/s), the mean fibre diameters of produced PVDF nanofibres were 530 nm, 420 nm, and 250 nm, respectively. By comparing the values of output air pressure (velocity), one can infer that turbulence plays a crucial role in defining fibre morphology. The obtained results will help in achieving a more tailored morphology of the fibres. The data presented here have been limited to PVDF but can be extended to other polymers with similar rheological properties.

Supplementary Materials: The following are available online at www.mdpi.com/article/10.3390/pr9061014/s1, Figure S1: (a–l) Air compressor dial gauge readings showing the input pressure values and the corresponding manometer output dynamic pressure values are shown immediately below, Figure S2: (a–l) Manometer readings when pitot tube was

placed at a distance of 0 mm from the nozzle end along the centreline, Figure S3: (a–l) Manometer readings when pitot tube was placed at a distance of 1 mm from the nozzle end along the centreline, Figure S4: (a–l) Manometer readings when pitot tube was placed at a distance of 2 mm from the nozzle end along the centreline, Figure S5: (a–l) Manometer readings when pitot tube was placed at a distance of 3 mm from the nozzle end along the centreline, Figure S6: (a–l) Manometer readings when pitot tube was placed at a distance of 5 mm from the nozzle end along the centreline, Figure S7: (a–l) Manometer readings when pitot tube was placed at a distance of 10 mm from the nozzle end along the centreline, Figure S8: (a–l) Manometer readings when pitot tube was placed at a distance of 20 mm from the nozzle end along the centreline, Figure S9: (a–l) Manometer readings when pitot tube was placed at a distance of 30 mm from the nozzle end along the centreline.

Author Contributions: Conceptualisation, I.S. and A.H.H.; methodology, R.A. and M.C.; software, M.C. and R.A.; validation, R.A., M.C., and J.M.; data curation, R.A. and M.C.; writing—original draft preparation, R.A.; writing—review and editing, R.A., M.C., J.K., J.M., A.H.H., N.S., E.E., and I.S.; supervision, I.S.; project administration, I.S.; funding acquisition, I.S. and A.H.H. All authors have read and agreed to the published version of the manuscript.

Funding: This research was funded by the British Council Grant Number 352360451 and Newton-Mosharafa Call between UK and Egypt, ID: 30886.

Institutional Review Board Statement: Not applicable.

Informed Consent Statement: Not applicable.

Data Availability Statement: Project data is stored at Edinburgh Napier University repository.

Acknowledgements: The authors would like to thank the British Council for providing funding for the Institutional Links Project (Project ID: 352360451) between Alexandria University, Egypt, and Northumbria University, Newcastle upon Tyne, UK. This work is part of the project (Newton-Mosharafa Call between UK and Egypt, ID: 30886) funded by the Science, Technology, and Innovation Funding Authority (STIFA), Egypt.

Conflicts of Interest: The authors declare no conflict of interest.

References

1. Atif, R.; Khaliq, J.; Combrinck, M.; Hassanin, A.H.; Shehata, N.; Elnabawy, E.; Shyha, I. Solution Blow Spinning of Polyvinylidene Fluoride Based Fibers for Energy Harvesting Applications: A Review. *Polymers* **2020**, *12*, 1304.
2. Tandon, B.; Kamble, P.; Olsson, R.T.; Blaker, J.J.; Cartmell, S.H. Fabrication and characterisation of stimuli responsive piezoelectric PVDF and hydroxyapatite-filled PVDF fibrous membranes. *Molecules* **2019**, *24*, 1903.
3. Medeiros, E.S.; Glenn, G.M.; Klaczynski, A.P.; Orts, W.J.; Mattoso, L.H.C. Solution Blow Spinning: A New Method to Produce Micro- and Nanofibers from Polymer Solutions. *J. Appl. Polym. Sci.* **2009**, *113*, 2322–2330.
4. Vural, M.; Behrens, A.M.; Ayyub, O.B.; Ayoub, J.J.; Kofinas, P. Sprayable elastic conductors based on block copolymer silver nanoparticle composites. *ACS Nano* **2015**, *9*, 336–344.
5. Behrens, A.M.; Casey, B.J.; Sikorski, M.J.; Wu, K.L.; Tutak, W.; Sandler, A.D.; Kofinas, P. In situ deposition of PLGA nanofibers via solution blow spinning. *ACS Macro Lett.* **2014**, *3*, 249–254.
6. Park, S.W.; Reitz, R.D. A gas jet superposition model for CFD modeling of group-hole nozzle sprays. *Int. J. Heat Fluid Flow* **2009**, *30*, 1193–1201.
7. Morrall, A.; Quayle, S.; Campobasso, M.S. Turbulence modelling for RANS CFD analyses of multi-nozzle annular jet pump swirling flows. *Int. J. Heat Fluid Flow* **2020**, *85*, 108652.
8. Xue, R.; Ruan, Y.; Liu, X.; Cao, F.; Hou, Y. The influence of cavitation on the flow characteristics of liquid nitrogen through spray nozzles: A CFD study. *Cryogenics* **2017**, *86*, 42–56.
9. Atif, R.; Shyha, I.; Inam, F. The degradation of mechanical properties due to stress concentration caused by retained acetone in epoxy nanocomposites. *RSC Adv.* **2016**, *6*, 34188–34197.
10. Drabek, J.; Zatloukal, M. Meltblown technology for production of polymeric microfibers/nanofibers: A review. *Phys. Fluids* **2019**, *31*, 091301.
11. Hassan, M.A.; Anantharamaiah, N.; Khan, S.A.; Pourdeyhimi, B. Computational Fluid Dynamics Simulations and Experiments of Meltblown Fibrous Media: New Die Designs to Enhance Fiber Attenuation and Filtration Quality. *Ind. Eng. Chem. Res.* **2016**, *55*, 2049–2058.
12. Wang, Y.; Wang, X. Investigation on a new annular melt-blowing die using numerical simulation. *Ind. Eng. Chem. Res.* **2013**, *52*, 4597–4605.
13. Moore, E.M.; Shambaugh, R.L.; Papavassiliou, D.V. Analysis of isothermal annular jets: Comparison of computational fluid dynamics and experimental data. *J. Appl. Polym. Sci.* **2004**, *94*, 909–922.

14. Han, W.; Xie, S.; Sun, X.; Wang, X.; Yan, Z. Optimization of airflow field via solution blowing for chitosan/PEO nanofiber formation. *Fibers Polym.* **2017**, *18*, 1554–1560.
15. Atif, R.; Combrinck, M.; Khaliq, J.; Hassanin, A.H.; Shehata, N.; Elnabawy, E.; Shyha, I. Solution Blow Spinning of High-Performance Submicron Polyvinylidene Fluoride Fibres: Computational Fluid Mechanics Modelling and Experimental Results. *Polymers* **2020**, *12*, 1140.
16. Zhang, L.; Shao, J.; Chen, X. CFD simulation of nozzle characteristics in a gas aggregation cluster source. *Vacuum* **2016**, *129*, 105–110.
17. Kimura, K. Chapter 3—Wind loads. In *Innovative Bridge Design Handbook*; Pipinato, A., Ed.; Butterworth-Heinemann: Boston, MA, USA, 2016; pp. 37–48.
18. Ren, G.; Liu, J.; Wan, J.; Li, F.; Guo, Y.; Yu, D. The analysis of turbulence intensity based on wind speed data in onshore wind farms. *Renew. Energy* **2018**, *123*, 756–766.
19. Arenas-López, J.P.; Badaoui, M. Stochastic modelling of wind speeds based on turbulence intensity. *Renew. Energy* **2020**, *155*, 10–22.
20. Lou, H.; Han, W.; Wang, X. Numerical study on the solution blowing annular jet and its correlation with fiber morphology. *Ind. Eng. Chem. Res.* **2014**, *53*, 2830–2838.